Physical Relation of Source I to IRc2 in the Orion KL Region [*]

Shin-ichiro OKUMURA,[1,2] Takuya YAMASHITA,[3] Shigeyuki SAKO,[4] Takashi MIYATA,[4]

Mitsuhiko HONDA,[5] Hirokazu KATAZA[6], and Yoshiko K. OKAMOTO[7]

[1]*Bisei Spaceguard Center, Japan Spaceguard Association,*

1716–3 Okura, Bisei-cho, Ibara-shi, Okayama 714–1411

[2]*Okayama Astrophysical Observatory, National Astronomical Observatory of Japan,*

Kamogata-cho, Asakuchi-shi, Okayama 719–0232

[3]*National Astronomical Observatory of Japan, 2–21–1 Osawa, Mitaka-shi, Tokyo 181–8588*

[4]*Institute of Astronomy, Graduate School of Science, University of Tokyo,*

2–21–1 Osawa, Mitaka-shi, Tokyo 181–0015

[5]*Department of Information Science, Kanagawa University,*

2946 Tsuchiya, Hiratsuka-shi, Kanagawa 259–1293

[6]*Institute of Space and Astronautical Science, Japan Aerospace Exploration Agency,*

3–1–1 Yoshinodai, Chuo-ku, Sagamihara-shi, Kanagawa 252–5210

[7]*Faculty of Science, Ibaraki University, 2–1–1 Bunkyo, Mito-shi, Ibaraki 310–8512*

okumura@spaceguard.or.jp

Abstract

We present mid-infrared narrow-band images of the Orion BN/KL region, and N-band low-resolution spectra of IRc2 and the nearby radio source "I." The distributions of the silicate absorption strength and the color temperature have been revealed with a sub-arcsecond resolution. The detailed structure of the 7.8 μm/12.4 μm color temperature distribution was resolved in the vicinity of IRc2. A mid-infrared counterpart to source I has been detected as a large color temperature peak. The color temperature distribution shows an increasing gradient from IRc2 toward source I, and no dominant temperature peak is seen at IRc2. The spectral energy distribution of IRc2 could be fitted by a two-temperature component model, and the "warmer component" of the infrared emission from IRc2 could be reproduced by scattering of radiation from source I. IRc2 itself is not self-luminous, but is illuminated and heated by an embedded luminous young stellar object located at source I.

---

[*] Based on data collected at Subaru Telescope and obtained from the SMOKA science archive, which is operated by the Astronomy Data Center, National Astronomical Observatory of Japan.

1. Introduction

The Orion Molecular Cloud, at a distance of 418 ± 6 pc (Kim et al. 2008), is the closest and best-studied region of massive star formation. After the discovery of BN (Becklin & Neugebauer 1967) and KL (Kleinmann & Low 1967), following infrared observations revealed that the KL nebula splits up into a number of compact "IRc" sources of different color temperatures (Rieke et al. 1973). The most luminous of these, IRc2, was thought to be the dominant energy source for the KL complex (Downes et al. 1981; Wynn-Williams et al. 1984).

Radio observations have detected H_2O masers (Hills et al. 1972; Sullivan 1973; Genzel & Downes 1977; Moran et al. 1977) and SiO masers (Snyder & Buhl 1974; Moran et al. 1977; Wright & Plambeck 1983) near IRc2, thought to be a common central point at that time. In addition, radio continuum point source "I" was found at the SiO maser position (Garay et al. 1987; Churchwell et al. 1987), and Menten & Reid (1995) pointed out that source I is located precisely at the centroid of the SiO maser distribution. Other observations also revealed that source I and SiO masers are surrounded by the H_2O "shell" masers (Genzel & Stutzki 1989; Wright et al. 1990; Gaume et al. 1998).

More recent high-resolution radio and infrared observations clarified that the infrared position of IRc2 is offset from the radio position of source I (Gezari 1992; Dougados et al. 1993; Menten & Reid 1995). Dougados et al. (1993) also resolved IRc2 into a number of components at 3.8 μm, suggesting the presence of several embedded stars. Gezari et al. (1998) estimated that the total infrared luminosity of IRc2 is only $L \sim 1000 L_\odot$, approximately 2 orders of magnitude lower than the previously accepted value. Therefore, it is generally accepted that IRc2 is not a very luminous single star which significantly contributes to the energetics of the KL complex.

The nature of IRc2, heated internally or externally, is still unclear. Intermediate cases were suggested, with some IRc2 components being self-luminous and others not (Gezari et al. 1998; Robberto et al. 2005). The external illuminating source has not been identified, though source I is a prime candidate. The relationship of source I to IRc2 also still remains ambiguous. In this paper, we present evidence of a direct linkage between IRc2 and source I with subarcsecond angular resolution mid-infrared data, and interpret that IRc2 is illuminated externally by source I.

2. Observations and Data Analysis

2.1. Observations and data acquisition

Mid-infrared imaging and spectroscopic observations of the Orion BN/KL region were made on 2002 January 2 and 2000 December 10, respectively, with the Cooled Mid-Infrared Camera and Spectrometer, COMICS (Kataza et al. 2000; Okamoto et al. 2003) mounted on the 8.2-m SUBARU telescope. The data were retrieved from the SUBARU archive system, SMOKA (Baba et al. 2002). Imaging observations were made in nine bands from 7.8 to 24.8 μm. The pixel scale was $0.''13$, and the total field of view was $31'' \times 41''$. To cancel the high background radiation, the secondary mirror chopping was used at a frequency of 0.5 Hz with a $30''$ throw and a direction to the position

Table 1. Parameters of the imaging observations on 2002 January 2

Object	Filter	Integ. Time	Air Mass	FWHM
	(μm)	(sec)		(arcsec)
BN/KL	7.8 ($\Delta\lambda = 0.7$)	19.6	1.349–1.311	0.40*
	8.8 ($\Delta\lambda = 0.8$)	39.8	1.285–1.264	0.43*
	9.7 ($\Delta\lambda = 0.9$)	39.2	1.242–1.215	0.44*
	10.5 ($\Delta\lambda = 1.0$)	40.2	1.205–1.188	0.46*
	11.7 ($\Delta\lambda = 1.0$)	39.7	1.180–1.165	0.46*
	12.4 ($\Delta\lambda = 1.2$)	39.7	1.159–1.146	0.42*
	18.5 ($\Delta\lambda = 0.9$)	4.8	1.396–1.451	0.66*
	20.8 ($\Delta\lambda = 0.9$)	7.9	1.484–1.509	0.70*
	24.8 ($\Delta\lambda = 1.9$)	3.8	1.524–1.559	0.96*
α CMi	7.8 ($\Delta\lambda = 0.7$)	1.0	1.284	0.39
	8.8 ($\Delta\lambda = 0.8$)	1.2	1.270	0.35
	9.7 ($\Delta\lambda = 0.9$)	1.0	1.265	0.59
	10.5 ($\Delta\lambda = 1.0$)	1.0	1.260	0.60
	11.7 ($\Delta\lambda = 1.0$)	1.0	1.240	0.43
	12.4 ($\Delta\lambda = 1.2$)	1.0	1.244	0.46
α Ori	18.5 ($\Delta\lambda = 0.9$)	1.0	1.338	0.53
	20.8 ($\Delta\lambda = 0.9$)	1.0	1.328	0.57
	24.8 ($\Delta\lambda = 1.9$)	1.0	1.315	0.65

* The image size measured for BN.

angle of $-90°$. A nodding technique was not used in the present observations because the object was bright enough compared to the fluctuation level of the remaining sky pattern after chopping subtraction. During imaging observations, α CMi and α Ori were observed for flux calibration. The full widths at half maximum (FWHMs) of the point spread function were measured to be $0.''35$–$0.''65$ for α CMi and α Ori. The parameters of our imaging observations are summarized in table 1. N-band low resolution ($\lambda/\Delta\lambda \sim 250$) spectroscopic observations were performed with the $0.''33$-wide, north-south slit. The pixel scale along the slit was $0.''165$. The observations were carried out on three slit positions in steps of $0.''33$ from west to east, on the eastern part of IRc2 including source I. During spectroscopic observations, the slit position was confirmed by referring to 8.8 μm slit-viewer images taken simultaneously. α Tau was observed and used for the correcting of the atmospheric absorption and flux calibration, based on Cohen et al. (1999). The parameters of our spectroscopic observations are summarized in table 2.

Table 2. Parameters of the spectroscopic observations on 2000 December 10

Object	Integ. Time (sec)	Air Mass	FWHM at 8.8μm (arcsec)	Resolution
IRc2	90.4[*]	1.285–1.231	0.63[†]	250
α Tau	4.0	1.076–1.071	0.50[‡]	250

[*] Total on-source integration time for each slit position.

[†] Measured for BN in the 8.8μm slit-viewer images.

[‡] Measured on the spectroscopic data.

2.2. Data reduction

The data were reduced by using IRAF [1] and our own reduction tools. For imaging data, after the standard chopping subtraction, the flat-fielding was carried out by using blank-sky images taken at the chopping-OFF (off-source) position. All flat-divided images were adjusted for the position referring to BN, with an accuracy of 0.1 pixel (corresponding to 0.″01), and then were co-added to produce a final image of size $\sim 28'' \times 36''$. For the spectroscopic data, after the procedure of chopping subtraction, the thermal spectra of the telescope cell-cover was used for flat-fielding. The wavelength scale was calibrated by atmospheric emission lines, and the distortion of the spectral image on the detector was corrected based on the spectra of the standard stars. The extracted spectra were divided by the spectrum of α Tau, which was in advance divided by a blackbody curve at a temperature of 4400 K.

2.3. Astrometric calibration

The astrometry has been determined with respect to the position of BN on the final co-added images. To register the radio position of source I (Menten & Reid 1995) and the 3.8 μm near-infrared positions (Dougados et al. 1993) on our images, we assumed that the radio, near-infrared, and mid-infrared centroids for BN were coincident, while BN is reported to have its own proper motions. Plambeck et al. (1995) formerly pointed out that BN and source I are moving apart at $\sim 0.''02$ yr^{-1}, and Rodríguez et al. (2005) presented the absolute proper motions of BN and source I. Gómez et al. (2005) determined the mean absolute motion of Orion, and registered all absolute proper motions to the "rest" frame of the Orion Nebula.

In applying the registration, the positions of BN and source I on other wavelength images were corrected to the positions on our images taken in 2002, by referring to the relative proper motions to the rest frame of the Orion Nebula, reported by Gómez et al. (2005): BN has a proper motion of 11.14±1.35 mas yr^{-1} to the northwest, while source I, 7.79±1.89 mas yr^{-1} to the southeast. In the registration, IRc2 is assumed to stand on the rest frame of the Orion Nebula. The astrometric correc-

[1] IRAF is distributed by the National Optical Astronomy Observatories, which is operated by the Association of Universities for Research in Astronomy (AURA), Inc., under cooperative agreement with the National Science Foundation.
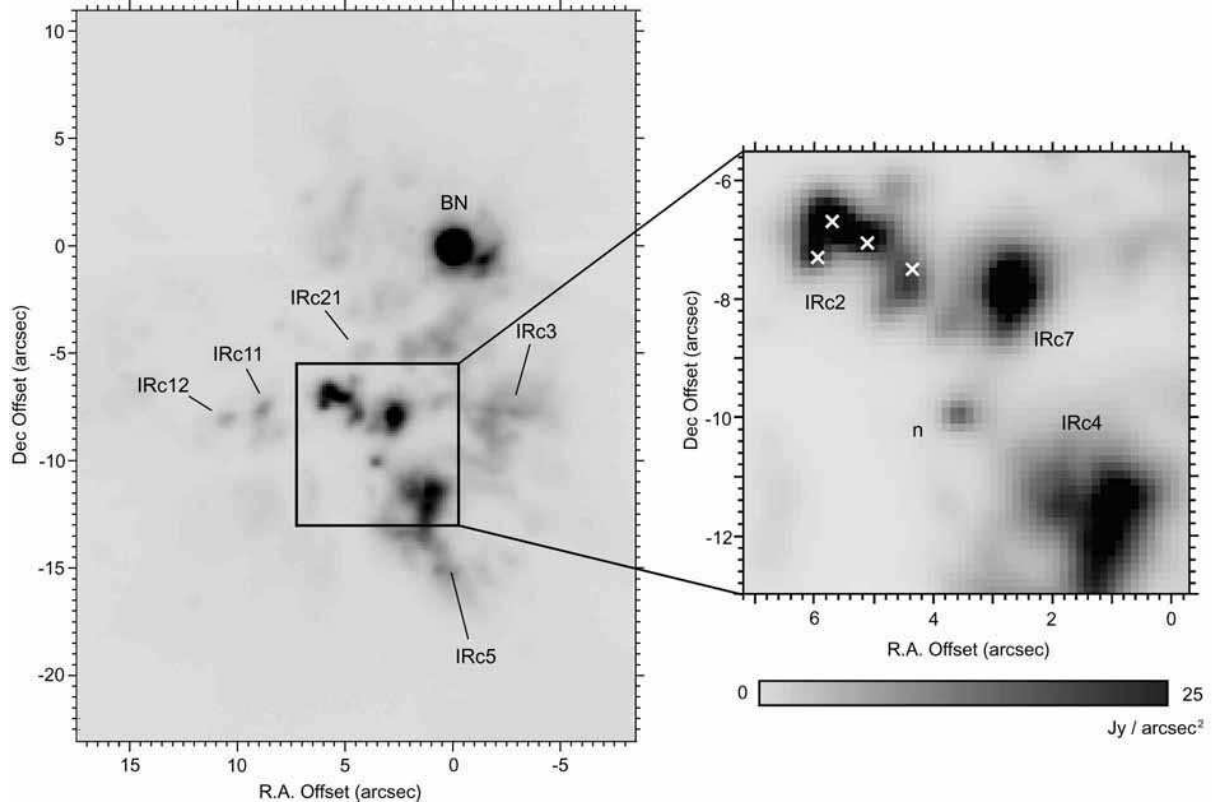
Fig. 1. 12.4 μm image of the $26'' \times 34''$ field of the BN/KL region (left) and the close-up image around IRc2 (right). Four crosses mark the positions of the 3.8 μm IRc2-A, B, D, C, from left to right (Dougados et al. 1993). Coordinates are centered on the BN object.

tions for individual sources amount to $0''.13$ in their maximum. The uncertainty in the registration, mainly caused by the proper motion, is estimated to be ≤ 1 pixel in our images.

3. Results

3.1. Morphology

Figure 1 shows a 12.4 μm image of the Orion BN/KL region ($26'' \times 34''$), and figure 2 gives a three-color (8.7 μm, 12.4 μm, and 18.5 μm) composite image of the same region. Our images agree well with the similar resolution mid-infrared data of Greenhill et al. (2004) or Shuping et al. (2004), taken at the Keck-I telescope with the Long-Wavelength Spectrometer. In figure 2, IR source n has a blue-color appearance, which represents a higher color temperature, whereas diffuse emission appears mostly to be red, which shows a lower color temperature. Several compact sources (IRc2, IRc12, IRc21, the southern part of IRc7, and the northern half of IRc11) stand out as greenish appearance in the image. No local peaks were detected at the source I position [(R.A., Dec.)$_{\text{offset}}$ = ($6''.0$, $-7''.7$) from BN], in any wavelength from 7.8 to 24.8 μm.

5
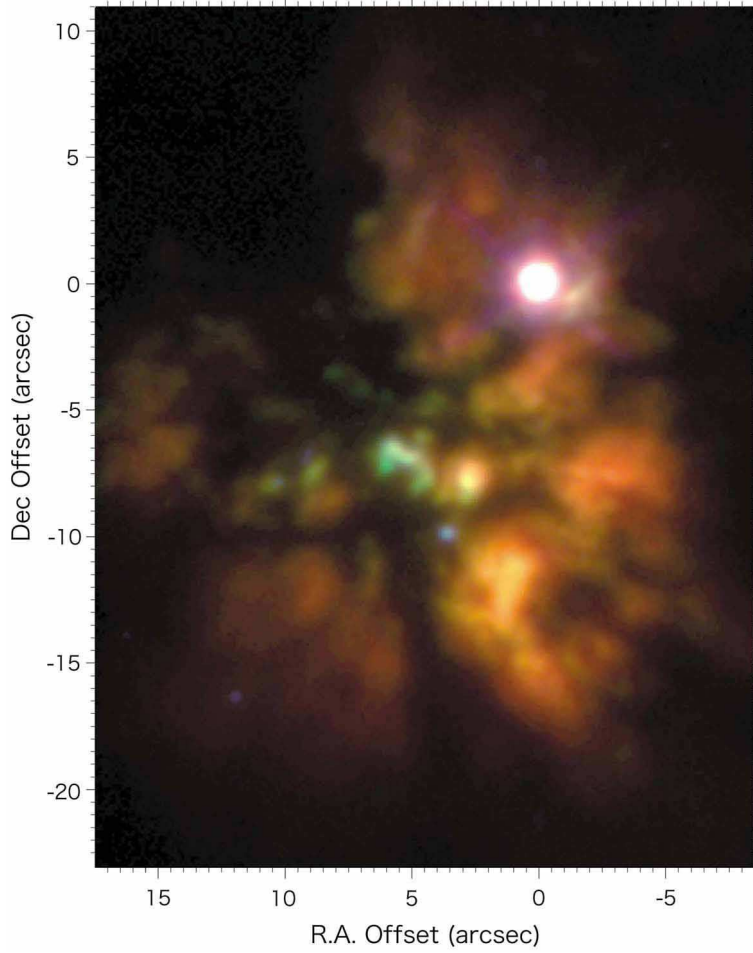
Fig. 2. Three-color composite image of the BN/KL region ($26''\times34''$): 8.7 μm (blue); 12.4 μm (green); and 18.5 μm (red).

3.2. *Silicate absorption and color temperature distribution around IRc2*

The strength of the 9.7 μm silicate absorption feature and the 7.8 μm/12.4 μm color temperature have been calculated for each pixel. The procedure is as follows:

1. The first-order 9.7 μm silicate absorption factor, $exp(\tau_{9.7})$, is approximated as the ratio of the observed 9.7 μm brightness to the 9.7 μm continuum, linearly interpolated between 7.8 and 12.4 μm.

2. The 7.8 and the 12.4 μm brightness are corrected (dereddened) based on the first-order 9.7 μm absorption factor. The dereddening corrections are performed by using the interstellar extinction low of $A_\lambda/A_V = 0.02$ (λ=7.8 μm) and 0.031 (λ=12.4 μm), interpolated from table 3 of Rieke & Lebofsky (1985). The ratio of $A_V/\tau_{Si} = 16.6$ (Rieke & Lebofsky 1985) was also used, where $\tau_{Si}=\tau_{9.7} + 0.03$, calculated from table 3 of Draine (1985) with the transmission curve of the COMICS 9.7 μm filter.

3. The first-order color temperature is approximated from the corrected 7.8 μm/12.4 μm brightness

6
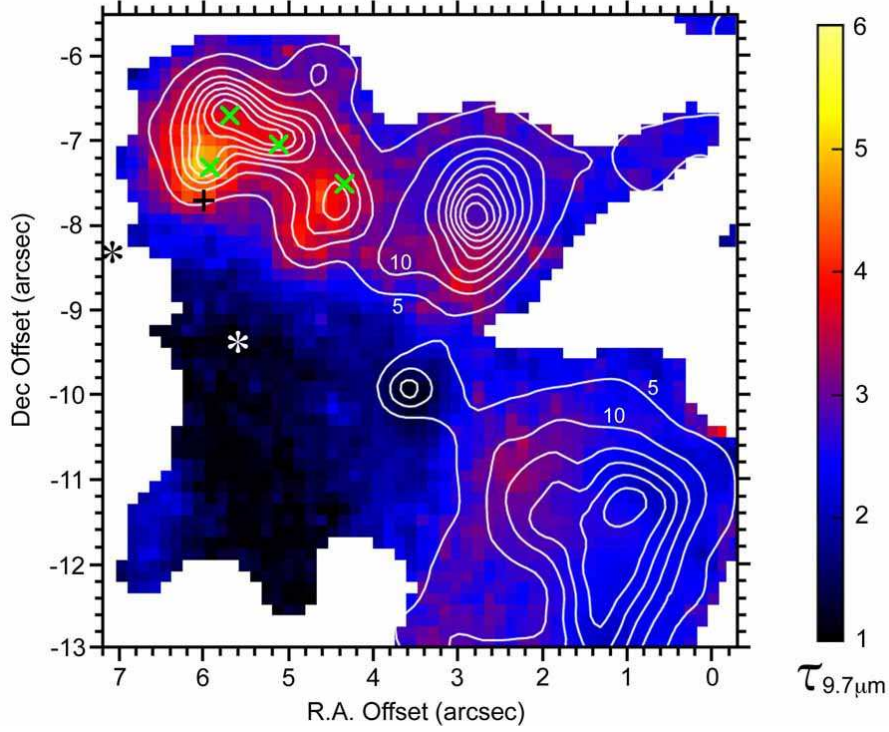
Fig. 3. 9.7 μm color-coded optical depth ($\tau_{9.7}$) image of the $7.''5 \times 7.''5$ field around IRc2. The color image is masked in the area of low S/N ratio (9.7 μm flux density ≤ 0.15 Jy/arcsec^2). The overlaid contour shows the 12.4 μm surface brightness, in steps of 5 Jy/arcsec^2. Four green crosses mark the positions of the 3.8 μm IRc2-A, B, D, C, from left to right (Dougados et al. 1993). A plus marks the position of radio source I (Menten & Reid 1995), corrected by referring to the proper motions presented by Gómez et al. (2005). A black asterisk shows the position of the "hot core" (Plambeck et al. 1982; Wright et al. 1992; Blake et al. 1996; Wilson et al. 2000) and a white asterisk denotes the 865 μm submillimeter continuum peak, SMA1 (Beuther et al. 2004). Symbol size indicates the uncertainty in its position. The coordinates are centered on BN.

ratio, assuming simple blackbody spectra [dust emissivity $\epsilon(\lambda)$=constant)].

4. The corrected absorption factor was calculated, as the ratio of the 9.7 μm brightness to the continuum, interpolated using the blackbody curve based on the first-order color temperature.

5. The 7.8 μm and the 12.4 μm brightness were again corrected by using the corrected absorption factor.

6. The final color temperature was calculated from the corrected 7.8 μm/12.4 μm ratio.

Figure 3 shows the 9.7 μm optical depth ($\tau_{9.7}$) distribution around IRc2. The error in the $\tau_{9.7}$ is estimated to be a maximum of 0.2. The average depth of IRc2 [$2.''5 \times 2.''0$ rectangular area centered on ($5.''4$, $-7.''2$)] is 3.8. We can see strong absorption in the vicinity of the 3.8 μm IRc2-A (Dougados et al. 1993). The peak of absorption ($\tau_{9.7} \sim 5.5$) occurs $0.''1$ east of IRc2-A; their positional separation is within our astrometric uncertainty.

Figure 4 shows the 7.8 μm/12.4 μm color temperature distribution around IRc2. The uncertainty in the corrected 7.8 μm/12.4 μm ratio is estimated at a maximum of 16 %. It corresponds to the

7
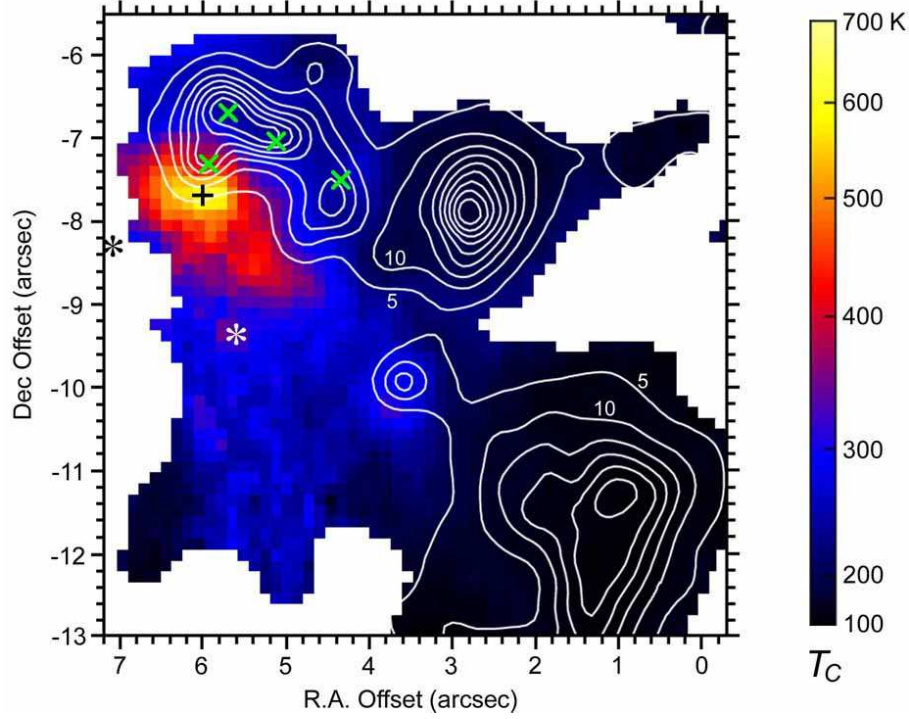
Fig. 4. 7.8 μm/12.4 μm color temperature distribution image of the $7''5 \times 7''5$ field around IRc2. The color image was omitted in the area of low S/N ratio. Contours, symbols, and coordinates are the same as in figure 3.

error of 10 K, 40 K, and 90 K at the color temperature of 200 K, 400 K, and 600 K. For the 12.4 μm IRc2 main-peak ($5''7$, $-6''7$), color temperature is 250 K, in agreement with an earlier result (Gezari et al. 1998), while the maximum color temperature, 650 K, occurs $\sim 1''$ south of the 12.4 μm IRc2 peak. The color temperature peak coincides with the position of source I within our astrometric error. We found another color temperature peak of 350 K at ($5''6$, $-9''4$), $1''9$ south-southwest of source I, corresponding to the 865 μm submillimeter continuum peak, SMA1 (Beuther et al. 2004).

3.3. Photometry

The mid-infrared flux densities of IRc2 and other sources were calculated from dereddened images. They are summarized in table 3, together with the near-infrared 4.0 μm flux densities by Dougados et al. (1993). A dereddening correction was computed using the interstellar extinction law of Rieke & Lebofsky (1985) and the dust grain optical constants of Draine (1985). The flux densities were integrated over the rectangles listed in the third column in table 3, while taking the flux density at ($5''5$, $-10''0$) as a background flux density for each wavelength. The typical photometric error is estimated to be approximately $\pm$ 5 %. The error is over 20 % in some cases, because of the low surface brightness, or contamination due to background plateau emission.

8

Source	Photometric Position* (arcsec)	Aperture† (arcsec)	Total Flux Density ‡ (Jy) 4.0§ (μm)	7.8 (μm)	8.8 (μm)	9.7 (μm)	10.5 (μm)	11.7 (μm)	12.4 (μm)	18.5 (μm)	20.8 (μm)	24.8 (μm)
BN	(0, 0)	3.4×3.4	220	420	670	640	630	740	700	*960*	*1500*	*1500*
Source n	(3.6, −9.9)	1.4×1.4	3.5	6.8	8.6	13	13	17	25	*<70*	*<140*	*<250*
IRc2-A	(6.0, −7.3)	0.7×0.7	4.2	63	65	84	66	78	110	*130*	*180*	*210*
IRc2-B	(5.8, −6.7)	0.7×0.7	1.8	28	55	49	49	79	100	*120*	*180*	*210*
IRc2-C	(4.5, −7.8)	0.7×0.7	1.9	16	20	28	32	47	61	*110*	*170*	*200*
IRc2-D	(5.3, −6.9)	0.7×0.7	0.6	22	46	39	40	66	86	*120*	*190*	*220*
IRc2 (Total)			8.5	130	190	200	190	270	360	*480*	*700*	*830*
IRc3	(−1.7, −7.6)	4.7×5.7	2.6	*12*	*28*	*52*	*110*	*220*	*310*	*2300*	4100	*5400*
IRc4	(1.1, −11.4)	4.3×4.0	⋯	*30*	45	100	180	380	530	2500	4200	5800
IRc5	(0.6, −15.0)	2.5×3.3	⋯	*2.7*	*7.1*	*14*	*33*	65	92	750	1400	1900
IRc7	(2.8, −7.9)	3.4×2.5	4.9	42	*60*	*94*	130	230	320	*1000*	1700	2300
IRc11	(8.9, −7.6)	3.5×2.3	⋯	*12*	*11*	25	*28*	40	67	*260*	*510*	830
IRc12	(10.5, −8.0)	2.0×1.7	⋯	7.8	8.5	14	17	21	29	*100*	*180*	*280*
Source I	(6.0, −7.7)‖	0.7×0.7	*<0.7*	*11*	5.5	*11*	9.6	7.8	*11*	*21*	*30*	*40*

* 12.4 μm peak position, offset from BN ($\Delta\alpha$, $\Delta\delta$).

† Rectangular size [(R.A.) × (Dec)].

‡ Typical photometric error is estimated to be approximately ± 5 %. It is sometimes over ± 20 % (in italics), because of low surface brightness and/or the surrounding plateau emission. At $\lambda > 18$ μm, source n is not distinct from its surrounding extended emission.

§ The flux densities at 4.0 μm are taken from Dougados et al. (1993), followed by the dereddening corrections in the procedures described in 3.2.

‖ Radio position (Menten & Reid 1995), corrected by the proper motion presented by Gómez et al. (2005).

3.4. Spectroscopy

Figure 5 presents the N-band low resolution spectra of IRc2, obtained at the positions of the 12.4 μm main-peak and radio source I. Except the silicate absorption, the spectra show no strong atomic or broad feature, such as the 8.6, 11.2, and 12.7 μm polycyclic aromatic hydrocarbon (PAH) features (e.g., Kassis et al. 2006), which would have affected the discussion in section 3.2. Figure 6 shows the 9.7 μm optical depth image (left) and the 7.8 μm/12.4 μm color temperature image (right) created from the spectra, through the same procedures discussed in section 3.2. The results are in agreement with figures 3 and 4.
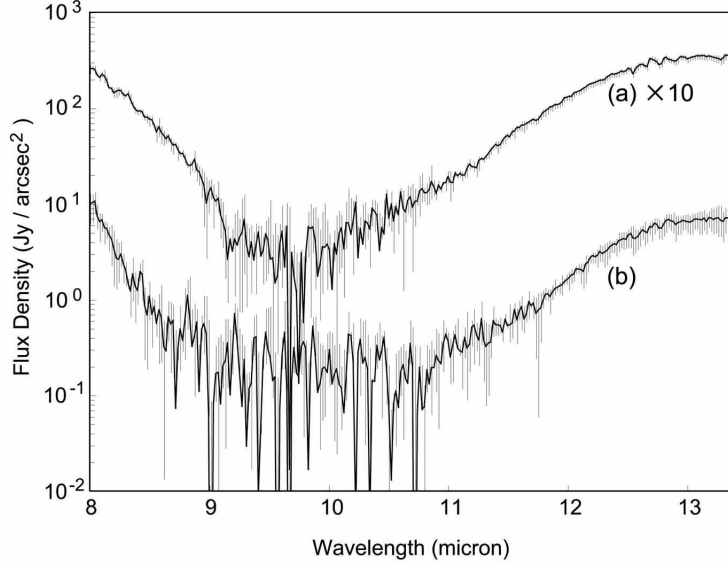
Fig. 5. N-band low resolution spectra of IRc2, at the position of 12.4 μm main-peak (a) and source I (b), shown in figure 6.
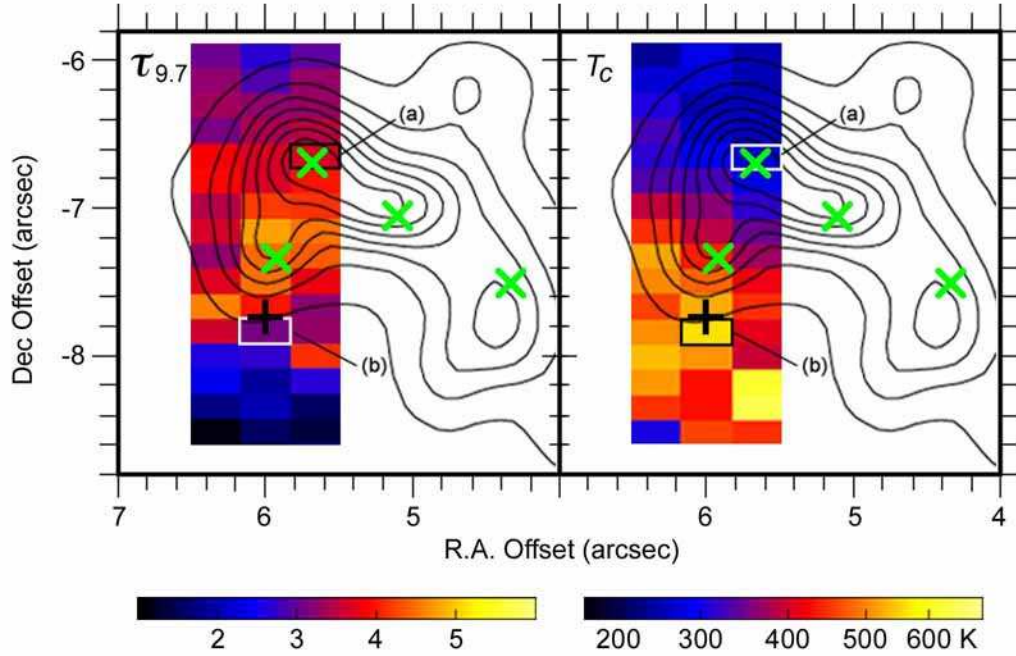
Fig. 6. 9.7 μm optical depth (left) and the 7.8 μm/12.4 μm color temperature (right) images of IRc2, constructed from the spectra. Overlaid contours and symbols are the same as in figure 3. The upper and lower spectra in figure 5 are obtained at the positions of (a) and (b), respectively.

4. Discussion

4.1. Background of the discussion about the relation between IRc2 and source I

The idea that IRc2 is a dominant energy source for the KL nebula was supported by early observations showing IRc2 to be associated with source I, within the positional errors at that time. Since IRc2 was found to be offset from radio source I, we have come to have many new discussions about the physical relation between IRc2 and source I. Gezari et al. (1998) revealed that the total infrared luminosity of IRc2 is only $L \sim 1000 L_\odot$, and concluded that IRc2 is a dense dust cloud heated internally by the near-infrared sources found by Dougados et al. (1993) and also externally by the luminous star at source I. They pointed out that a silicate absorption peak and a color temperature peak both occur near IRc2, whereas the detailed structure of the distribution of absorption and color temperature in the vicinity of IRc2 was not fully resolved from their $1.''1$-FWHM resolution data, because IRc2 is in close proximity ($\sim 1''$) of source I. For example, their maximum silicate absorption factor (9.8 μm line-to-continuum ratio), 52, is reproduced by the average optical depth of IRc2 in our result. Greenhill et al. (2004) speculated that knots in IRc2 as well as source I are individual sites of star formation. In support of this speculation, they noted that the relative distributions of emission in IRc2 from 2.2 μm to 22 μm do not exhibit an overall systematic pattern, such as central heating by one or two dominant energy sources. They also mentioned that from among all knots in IRc2, only IRc2-C is associated with a cluster of OH masers and X-ray emission. Shuping et al. (2004) pointed out that the near-infrared IRc2 knots all appear on the periphery of the 12.5 μm emission. They also pointed out that the volume-averaged density for IRc2 would be much larger than that of a typical star-forming cloud core, if IRc2 knots were all embedded protostars. For these reasons, they suggested the possibility that IRc2 is illuminated and heated by source I, whereas they also suggested another possibility that both external and internal heating play a role in the emission from IRc2, as would be expected if a low mass, dense protostar cocoon are placed close to an energy source. Robberto et al. (2005) resolved a conspicuous point source at the location of the IRc2-A knot in their dereddened mid-infrared images. They considered a possibility that source I and IRc2-A are representing deeply embedded individual sources, and that other IRc2 knots are diffuse sources heated externally by IRc2-A.

4.2. Dereddened spectral energy distributions of IRc2 and other sources

Figure 7 shows the dereddened 4–24.8 μm spectral energy distributions (SEDs) of some sources listed in table 3, together with the curves of Planck functions fitted to the SEDs. Although the SED of BN cannot be reproduced by a single blackbody emission, it can be fitted by a two-temperature component model, e.g., 600 K and 150 K. The SED of source n, already identified to be a stellar object with a circumstellar disk (Shuping et al. 2004; Greenhill et al. 2004), is also reproduced by a similar model. In contrast, the SEDs of IRc4 and IRc5 can be reproduced by single temperature components at 140 K and 120 K, respectively. It is a plausible conclusion that IRc4 and IRc5 are
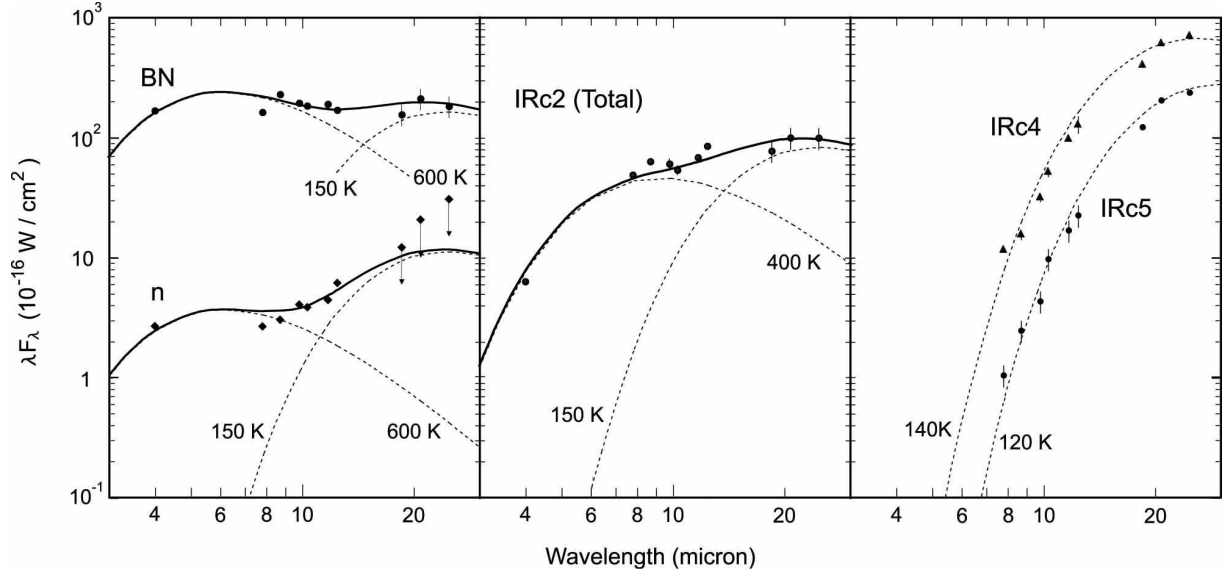
Fig. 7. Dereddened spectral energy distributions (SEDs) of BN and source n (left panel), IRc2 (middle panel), and IRc4 and IRc5 (right panel). Dashed curves show single temperature Planck functions. Solid curves show the sum of the dashed curves in each panel.

simple dust clouds heated by an external energy source(s). The SED of IRc2 cannot be reproduced by a single blackbody model; a warmer component (e.g., 400 K) seems to overlap a cooler component (e.g., 150 K), similar to that of BN or source n. In its appearance, IRc2 seems to be a self-luminous object. In the following section, however, we describe the origin of the "warmer component" in the SED of IRc2, which shows that IRc2 is not self-luminous.

4.3. Physical relation of source I to IRc2

In this subsection, we discuss the origin of the "warmer component" of the emission from IRc2. The simplest interpretation, widely accepted for $\sim$ 30yr, is the presence of an internal heating source. In figure 4, however, the highest color temperature peak occurs at source I, $1''$ south of the 12.4 μm peak of IRc2, and a local color temperature distribution has increasing gradients from IRc2-B, C, and D toward source I. Figure 8 shows the extinction-corrected 7.8 μm/12.4 μm brightness ratio contour map. It is a color temperature map similar to figure 4, whereas it displays weaker levels to clearify the detailed structure around IRc2. The 7.8 μm/12.4 μm brightness ratios for IRc2-B, C, and D are approximately 0.3. They are only 24 % of the ratio for source I and correspond to the color temperature of $\sim$ 265 K. A small peak of the color temperature is seen near to the westernmost component, IRc2-C, but no peak is near IRc2-B and D. No temperature peak is seen near IRc2-A, because it is probably overlapped by the shoulder of the large peak at source I.

A temperature peak should indicate the location of a luminosity source, on the argument that temperature gradients trace the direction of energy flow. Therefore, the color temperature distribution suggest a luminosity source at the position of source I. The temperature distribution does not necessarily rule out the possibility of other self-luminous sources embedded in the location where no

12
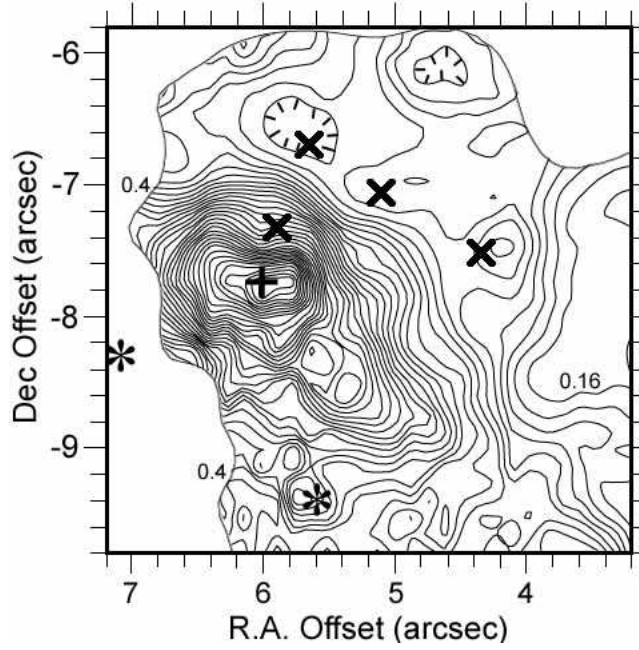
Fig. 8. Extinction-corrected 7.8 μm/12.4 μm brightness ratio contour map of the $4'' \times 4''$ field around IRc2. Four crosses mark the positions of the 3.8 μm IRc2-A, B, D, C, from left to right. A plus and two asterisks mark the positions of the radio source I, the hot core, and SMA1, same as in figure 3. The contour step is 0.03. The contour was omitted in the area of low S/N ratio.

temperature peak is seen. However, if there are other dominant luminosity sources within IRc2, they must be obscured by the large extinction that makes even the structure of the local color temperature peak surrounding them invisible. Therefore, we conclude that no dominant self-luminous object is embedded in IRc2, though faint self-luminous sources may be embedded.

As previously presented in subsection 3.2, the 3.8 μm emission peak, IRc2-A, coincides with the absorption peak. It is surprising that the shorter wavelength emission exhibits its intensity peak at the local absorption peak position, when the 3.8 μm emission arises from self-luminous objects deeply embedded in IRc2-A. This naturally leads to the interpretation that near-infrared emission from IRc2-A is due to scattering of radiation from an external source; source I is the most likely candidate. Two other near-infrared IRc2 knots, IRc2-B and D, also reflect surface layers of dense clouds illuminated by an external source. There remains the possibility that a faint self-luminous object to be embedded in IRc2-C. However, it is not easy to conclude that the object is a dominant energy source of IRc2.

Previous polarimetric observations by Dougados et al. (1993) show that IRc2-A and IRc2-B are highly polarized at 3.8 μm (14% and 17%, respectively), with position angles practically perpendicular to the direction of source I. Their results support the suggestion that IRc2-A and IRc2-B are illuminated under conditions of single scattering by source I, but not by IRc2-C. Low polarization of 8.3 % for IRc2-C (Dougados et al. 1993) suggests the possibility of IRc2-C is self-luminous.

For helping the discussion concerning the origin of the warmer component in the SED of IRc2, the IRc2 contour maps at 7.8 μm and 20.4 μm are presented in figure 9, together with the near-

13
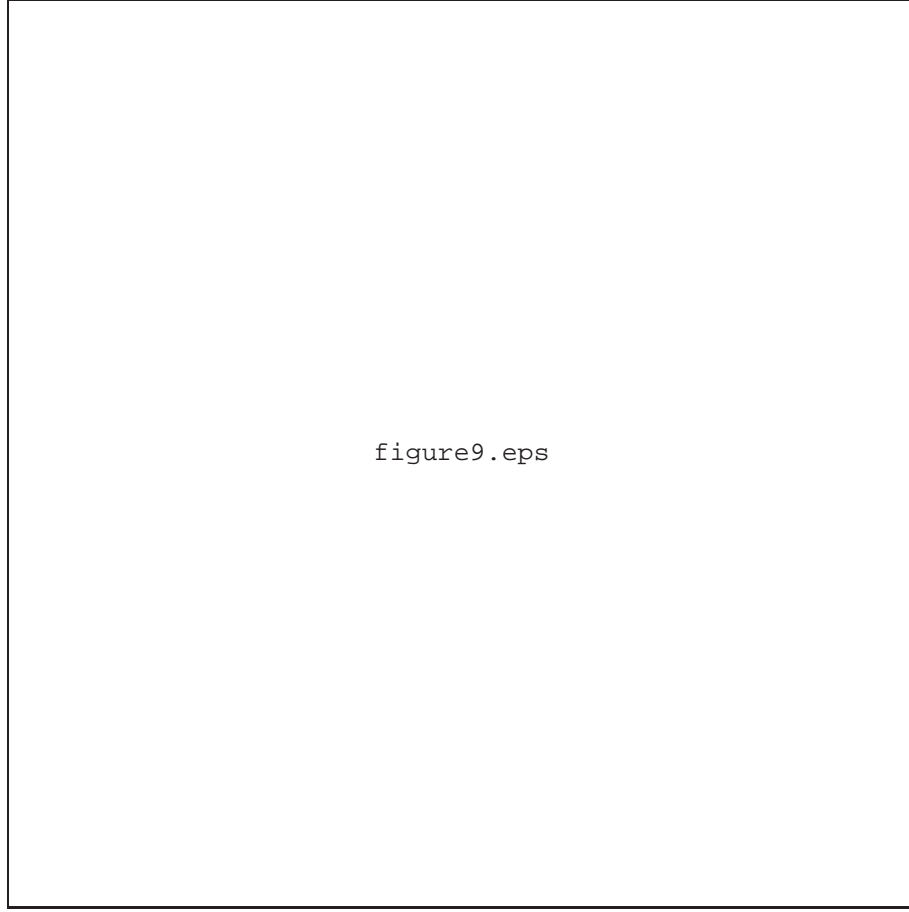
Fig. 9. Contour maps of IRc2 and neighboring sources: (a) 7.8 μm contour map. The contours start at 2 Jy/arcsec^2 and continue in steps of 4 Jy/arcsec^2. (b) 20.4 μm contour map. The contours start at 5 Jy/arcsec^2, runnning in steps of 10 Jy/arcsec^2. (c) 5.0 and 4.0 μm contour map from Dougados et al. (1993). (d) 9.7 μm optical depth map. The contour levels are from 2.0 to 5.3 Jy/arcsec^2 in steps of 0.3 Jy/arcsec^2. The map is masked in the area of low S/N ratio. Symbols are the same as in figure 8.

infrared contour map of Dougados et al. (1993) and the 9.7 μm optical depth distribution. The images at 7.8 μm and 20.4 μm roughly correspond to the spatial distributions of the warmer component and the cooler component, respectively. In figure 9, the cooler component is dominant at IRc4 and IRc7, whereas both the warmer component and the cooler component are found at IRc2, as previously noted in subsection 4.2. The appearances of IRc2 are different in each image of 7.8 μm and 20.4 μm, which shows a possibility that the sources of the warmer component and the cooler component are different. The origin of the cooler component is certainly reradiation from dust cloud. It is also the case with IRc4 and IRc5 as discussed in subsection 4.2. For IRc2, a morphological correlation is seen between the 7.8 μm image and the near-infrared 4.0 μm/5.0 μm image of Dougados et al. (1993). In figure 9, in addition, it is easy to recognize a close correlation between the 7.8 μm image and the optical depth distribution at IRc2.

We suggest that the warmer component of the mid-infrared emission from IRc2 arises from

14
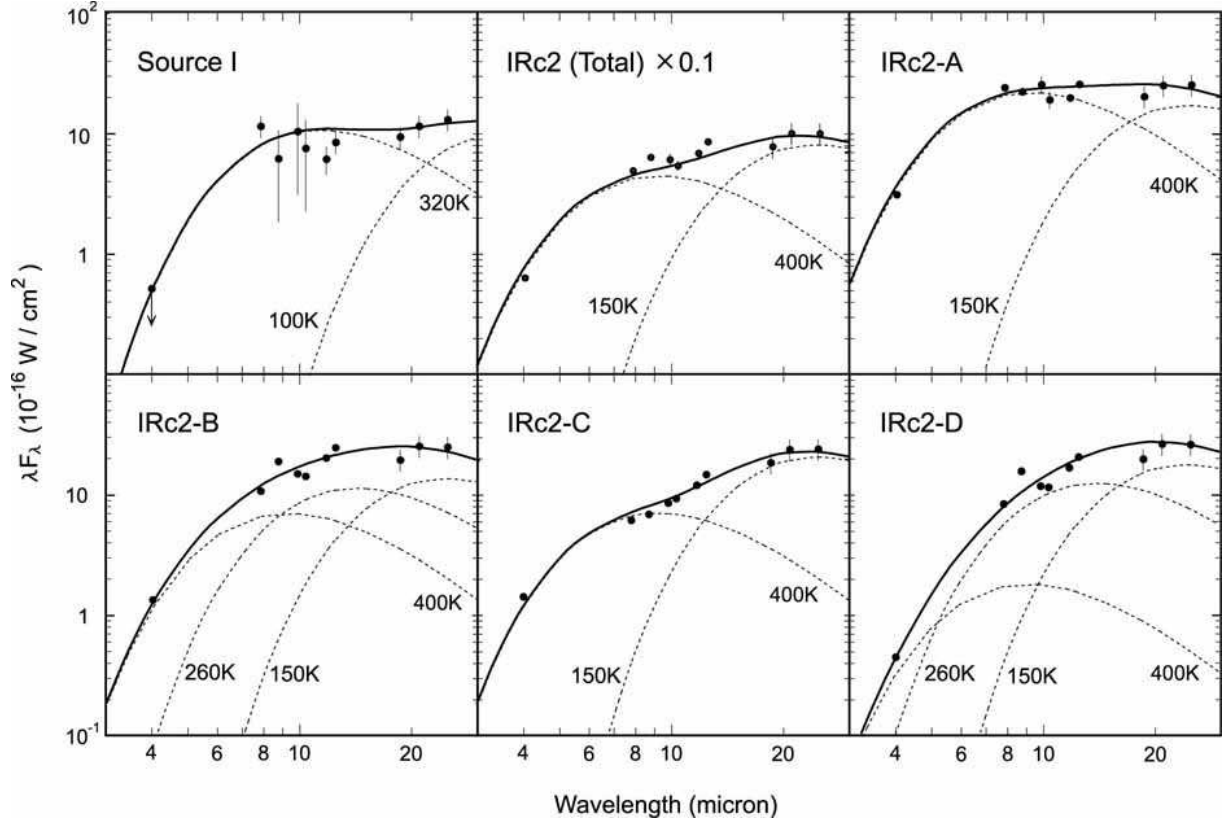
Fig. 10. Dereddened spectral energy distributions (SEDs) of source I and individual IRc2 knots. Dashed curves show single-temperature Planck functions, and solid curves show the sum of the dashed curves.

the same source as the near-infrared emission. This means that the mid-infrared warmer component emission from IRc2 is the scattering of radiation from source I. Then, the warmer component emission should suffer not only line-of-sight extinction, but also significant amounts of extinction along the path from source I to IRc 2. This is consistent with a larger optical depth of IRc2, and also with the morphological coincidence between the 7.8 μm image and the optical depth distribution of IRc2.

Figure 10 shows the dereddened SEDs of source I and total and individual IRc2 knots. The SEDs of IRc2-A and IRc2-C can be reproduced by the combination of a warmer component (400 K) and a cooler component (150 K). Here, we must note that the previously presented 7.8 μm/12.4 μm color temperature (figures 4, 6, and 8) is estimated based on the total amount of each temperature component. It can be easily recognized that the cooler component represents emission from the dust cloud heated externally. We will discuss the origin of the warmer component based on a suggestion that it is scattered light. For "astronomical silicate," the scattering efficiency generally decreases with wavelength in the infrared region. At 8 μm $< \lambda <$ 10 μm, however, the scattering efficiency increases with wavelength; the efficiency at 12.4 μm is 1.7 times larger than that at 7.8 μm (Draine & Lee 1984; Draine 1985). Therefore, scattering process brings a reddening effect to the SED at this wavelength. It leads to a decrease in the 7.8 μm/12.4 μm color temperature; the 7.8 μm/12.4 μm brightness ratio of 1.10 for the unit of W cm^{-2}, which corresponds to the color temperature of

400 K, can be explained by scattering of the radiation with the original 7.8 μm/12.4 μm ratio of 1.87, which indicates a color temperature of 600 K. Therefore, the 400 K warmer component in the SED can be explained by the result of the scattering of 600 K blackbody radiation in this wavelength region. IRc2-B and IRc2-D cannot be reproduced by a two-component blackbody model. Another blackbody component (e.g., 260 K) seems to be overlapped on the two-component model, though it is of unclear origin. There are some possibilities; a multiple scattering effect, the presence of hot dust, or the presence of deeply embedded sources.

Though the SED of source I cannot be easily fitted by a single- or a two-temperature component model, it is roughly reproduced by a combination of a 320 K component and a 100 K component. The SED probably represents the radiation from hot dust heated by source I, but not from (embedded) source I, itself. Therefore, the extinction toward source I is estimated to be smaller than that toward IRc2. Direct emission from source I is concealed by dense dust, and in the mid-infrared region, it is visible only as the scattered light from IRc2.

Mid-infrared spectropolarimetric observations of IRc2 were reported by Aitken et al. (1993), Aitken et al. (1997), and Smith et al. (2000). Their observations, with an aperture of 2″9 diameter, showed that the polarization position angles of IRc2 at 8 μm, 10 μm, and 12 μm were 73±4°, 130±20°, and 90±2°, respectively (Smith et al. 2000). They proposed a polarization mechanism of a two-component model due to dichroic absorption and emission processes by aligned grains, to explain variations of the polarization fraction and position angle. They argued that the observed polarization of IRc2 was reproduced by combining the absorptive component with a position angle of 120° and the emissive component with 60° (Aitken et al. 1997). Figure 11 shows the mid-infrared polarization and the undereddened surface brightness of IRc2. At 8 μm and 12 μm, we infer that the scattering effect plays a considerable role in the polarization mechanism of IRc2, whereas the 10 μm polarization is thought to be predominantly due to dichroic absorption showing the direction of an overlying magnetic field of ∼120° (Aitken et al. 1997), because (presumed) scattered emission is too weak to contribute to the polarization mechanism.

We conclude that the mid-infrared emission from IRc2, especially the warmer component in the SED, is scattered light that originally arises from source I, because (1) no dominant color temperature peak is seen at IRc2, (2) the near-infrared emission from IRc2 is most likely to be scattered radiation because of large polarization, and also a good correlation is seen in the appearance of IRc2 between the mid-infrared warmer component and the near-infrared emission, (3) a good correlation between the distribution of optical depth and the appearance of the warmer component is seen at IRc2, and (4) the warmer component can be reproduced by reddening process in scattering of emission from source I. Therefore, IRc2 itself, is not a dominant luminosity source, and also not a dominant energy source of KL, though some faint self-luminous objects may be embedded.
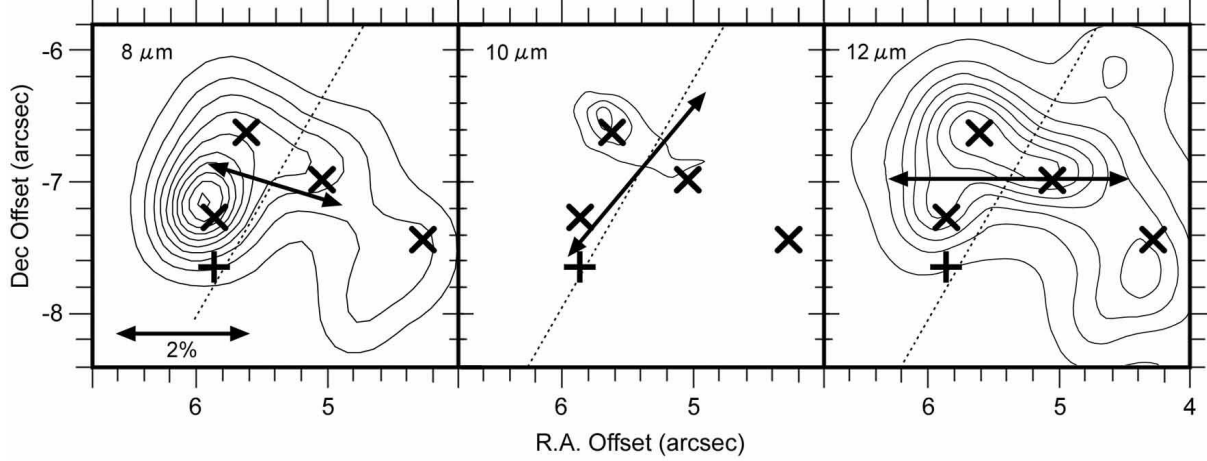
Fig. 11. Polarization vectors of IRc2 at 8 μm (left), 10 μm (middle), and 12 μm (right), obtained in 1990 with an aperture of 2.″9 diameter (Smith et al. 2000). Dotted lines show the overlying magnetic field direction (Aitken et al. 1997). Overlaid contour maps represent the undereddened surface brightness at 7.8 μm (left), 9.7 μm (middle), and 12.4 μm (right), respectively. The contour levels are from 2 to 22 Jy/arcsec^2 in steps of 4 Jy/arcsec^2 (left), 0.5, 0.6, 0.7 Jy/arcsec^2 (middle), and from 5 to 40 Jy/arcsec^2 in steps of 5 Jy/arcsec^2 (right). Four crosses and a plus mark the positions of the 3.8 μm IRc2 knots and source I, same as in figure 6 or figure 8. They are corrected to those in the epoch of 1990, referring to the proper motions by Gómez et al. (2005).

4.4.   Comparison with recent radio observations

Recent millimeter observations revealed the existence of a "hot core," with an estimated temperature of 350 K (Beuther et al. 2005), 1.″2 southeast from source I. However, no mid-infrared counterpart to the hot core has been detected, probably due to high extinction. In contrast to the hot core, the submillimeter continuum peak SMA1 is detected as a color temperature peak in figures 4 and 8, though we cannot identify any counterpart to SMA1 at each wavelength image. SMA1 is a protostellar object concealed by dense dust, just like source I.

Reid et al. (2007) and Matthews et al. (2010) proposed that source I has an edge-on disk whose rotation axis is oriented along northeast-southwest (NE-SW). The newly proposed NE-SW axis is different from the northwest-southeast (NW-SE) axis previously proposed in 1980's (Hasegawa et al. 1984). As Testi et al. (2010) pointed out, the NE-SW axis disk model is hard to reconcile with the observed NW-SE direction of the large-scale outflow cavity (e.g., Erickson et al. 1982), under the hypothesis that the disk is responsible for the bipolar outflow that blows in the direction of the axis of the disk. Our model, that IRc2 represents the scattering of radiation from source I, also seems to be inconsistent with the new NE-SW axis disk model, because IRc2 is approximately located northwest of source I. However, the inconsistency is canceled when the dominant illuminator of IRc2 is the rotating disk around source I rather than the photosphere of its central star, while the surrounding near-infrared nebulosity is due to reflection of the light from the photosphere (Morino et al. 1998; Testi et al. 2010).

As noted in subsection 2.3, the proper motions of BN, source I, and source n were reported by

17

many authors and the dynamical history of the Orion BN/KL region was also discussed. There are claims that the large-scale high-velocity outflow is not the typical one powered by a disk accretion. Gómez et al. (2008) proposed that a dynamical decay of a protostellar cluster resulted in the formation of a tight binary (source I) and the high-velocity ejection of BN and source n. Then, Bally et al. (2011) proposed that the gravitational potential energy released by the formation of the source I binary resulted in the stellar ejection, and also powered large-scale outflow. Goddi et al. (2011) presented another scenario that source I originally existed as a softer binary and that the gravitational energy was released in the process of hardening of the softer binary, after a dynamical interaction between source I and BN. The proper motion study of IRc2, e.g., relative to source I, will be helpful information for discussing the evolutional history of source I and the origin of the high-velocity outflow.

5. Conclusion

In this paper we present mid-infrared imaging and spectroscopic data of the Orion BN/KL region. The distributions of silicate absorption strength and color temperature were calculated around IRc2 with our $0''.4$-resolution data. The detailed structure of the color temperature distribution around IRc2, including source I and SMA1, has been revealed in the mid-infrared region for the first time. In the vicinity of IRc2, the peak color temperature occurs at source I, and an increasing temperature gradient is seen from IRc2 toward source I. The warmer component of the mid-infrared emission from IRc2 can be reproduced by the scattering of radiation from source I. IRc2, itself, is not a self-luminous object, but illuminated and heated by an external source, an embedded young stellar object located at source I.

References

Aitken, D. K., Wright, C. M. Smith, C. H., & Roche, P. F. 1993, MNRAS, 262, 456

Aitken, D. K., Smith, C. H., Moore, T. J. T., Roche, P. F., Fujiyoshi, T., & Wright, C. M. 1997, MNRAS, 286, 85

Baba, H., et al. 2002, ADASS XI, ed. D. A. Bohlender, D. Durand, & T. H. Handley, ASP Conference Series, Vol.281, 298

Bally, J., Cunningham, N. J., Moeckek, N., Burton, M. G., Smith, N., Frank, A., & Nordlund, A. 2011, ApJ, 727, 113

Becklin, E. E., & Neugebauer, G. 1967, ApJ, 147, 799

Beuther, H., et al. 2004, ApJ, 616, L31

Beuther, H., et al. 2005, ApJ, 632, 355

Blake, G. A., Mundy, L. G., Carlstrom, J. E., Padin, S., Scott, S. L., Scoville, N. Z., & Woody, D. P. 1996, ApJ, 472, L49

Churchwell, E., Felli, M., Woods, D. O. S., & Massi, M. 1987, ApJ, 321, 516

Cohen, M., Walker, R. G., Carter, B., Hammersley, P., Kidger, M., & Noguchi, K. 1999, AJ, 117, 1864

Dougados, C., Lena, P., Ridgway, S. T., Christou, J. C., & Probst, R. G. 1993, ApJ, 406, 112

Downes, D., Genzel, R., Becklin, E. E., & Wynn-Williams, C. G. 1981, ApJ, 244, 869

Draine, B. T., & Lee, H. M. 1984, ApJ, 285, 89

Draine, B. T. 1985 ApJS, 57, 587

Erickson, N. R., Goldsmith, P. F., Snell, R. L., Berson, R. L., Huguenin, G. R., Ulich, B. L., & Lada, C. J. 1982, ApJ, 261, L103

Garay, G., Moran, J. M., & Reid, M. J. 1987, ApJ, 314, 535

Gaume, R. A., Wilson, T. L., Vrba, F. J., Johnston, K. J., & Schmid-Burgk, J. 1998, ApJ, 493, 940

Genzel, R., & Downes, D. 1977, A&A, 61, 117

Genzel, R., & Stutzki, J. 1989, ARA&A, 27, 41

Gezari, D. Y. 1992, ApJ, 396, L43

Gezari, D. Y., Backman, D. E., & Werner, M. W. 1998, ApJ, 509, 283

Goddi, C., Humphreys, E. M. L., Greenhill, L. J., Chandler, C. J., & Matthews, L. D. 2011, ApJ, 728, 15

Gómez, L., Rodríguez, L. F., Loinard, L., Lizano, S., Poveda, A., & Allen, C. 2005, ApJ, 635, 1166

Gómez, L., Rodríguez, L. F., Loinard, L., Lizano, S., Allen, C., Poveda, A., & Menten, K. M. 2008, ApJ, 685, 333

Greenhill, L. J., Gezari, D. Y., Danchi, W. C., Najita, J., Monnier, J. D., & Tuthill, P. G. 2004, ApJ, 605, L57

Hasegawa, T., et al. 1984, ApJ, 283, 117

Hills, R., Janssen, M. A., Thornton, D. D., & Welch, W. J. 1972, ApJ, 175, L59

Kassis, M., Adams, J. D., Campbell, M. F., Deutsch, L. K., Hora, J. L., Jackson, J. J., & Tollestrup, E. V. 2006, ApJ, 637, 823

Kataza, H., Okamoto, Y., Takubo, S., Onaka, T., Sako, S., Nakamura, K., Miyata, T., & Yamashita, T. 2000, Proc. SPIE, 4008, 1144

Kim, M. K., et al. 2008, PASJ, 60, 991

Kleinmann, D. E., & Low, F. J. 1967, ApJ, 149, L1

Matthews, L. D., Greenhill, L. J., Goddi, C., Chandler, C. J., Humphreys, E. M. L., Kunz, M. W. 2010, ApJ, 708, 80

Menten, K. M., & Reid, M. J. 1995, ApJ, 445, L157

Moran, J. M., Johnston, K. J., Spencer, J. H., & Schwartz, P. R. 1977, ApJ, 217, 434

Morino, J.-I., Yamashita, T., Hasegawa, T., & Nakano, T. 1998, Nature, 393, 340

Okamoto, Y. K., Kataza, H., Yamashita, T., Miyata, T., Sako, S., Takubo, S., Honda, M., & Onaka, T. 2003, Proc. SPIE, 4841, 169

Plambeck, R. L., Wright, M. C. H., Welch, W. J., Bieging, J. H., Baud, B., Ho, P. T. P., & Vogel, S. N. 1982, ApJ, 259, 617

Plambeck, R. L., Wright, M. C. H., Mundy, L. G., & Looney, L. W. 1995, ApJ, 455, L189

Reid, M. J., Menten, K. M., Greenhill, L. J., & Chandler, C. J. ApJ, 664, 950

Rieke, G. H., Low, F. J., & Kleinmann, D. E. 1973, ApJ, 186, L7

Rieke, G. H., & Lebofsky, M. J. 1985, ApJ, 288, 618

Robberto, M., et al. 2005, AJ, 129, 1534

Rodríguez, L. F., Poveda, A., Lizano, S., & Allen, C. 2005, ApJ, 627, L65

Shuping, R. Y., Morris, M., & Bally, J. 2004, AJ, 128, 363

Smith, C. H., Wright, C. M. Aitken, D. K., Roche, P. F., & Hough, J. H. 2000, MNRAS, 312, 327

Snyder, L. E., & Buhl, D. 1974, ApJ, 189, L31

Sullivan, W. T. 1973, ApJS, 25, 393

Testi, L., Tan, J. C., & Palla, F. 2010, A&A, 522, 44

Wilson, T. L., Gaume, R. A., Gensheimer, P., & Johnston, K. J. 2000, ApJ, 538, 665

Wright, M. C. H., & Plambeck, R. L. 1983, ApJ, 267, L115

Wright, M. C. H., Carlstrom, J. E., Plambeck, R. L., & Welch, W. J. 1990, AJ, 99, 1299

Wright, M. C. H., Sandell, G., Wilner, D. J., & Plambeck, R. L. 1992, ApJ, 393, 225

Wynn-Williams, C. G., Genzel, R., Becklin, E. E., & Downes, D. 1984, ApJ, 281, 172